A&A 592, A104 (2016)
DOI: 10.1051/0004-6361/201628467

Astronomy & Astrophysics

XMM-Newton reveals a Seyfert-like X-ray spectrum in the z = 3.6 QSO B1422+231

M. Dadina[1], C. Vignali[2], M. Cappi[1], G. Lanzuisi[2,3], G. Ponti[4], B. De Marco[4], G. Chartas[5], and M. Giustini[6]

[1] INAF/IASF Bologna via Gobetti 101, 40129 Bologna, Italy
e-mail: dadina@iasfbo.inaf.it
[2] Dipartimento di Fisica e Astronomia dell'Universitá degli Studi di Bologna, via Ranzani 1, 40127 Bologna, Italy
[3] INAF Osservatorio astronomico di Bologna, via Ranzani 1, 40127 Bologna, Italy
[4] Max-Planck-Institut für Extraterrestrische Physik, Giessenbachstrasse 1, 85748 Garching, Germany
[5] Department of Physics and Astronomy of the College of Charleston, Charleston, SC 29424, USA
[6] SRON Netherlands Institute for Space Research, Sorbonnelaan 2, 3584 CA Utrecht, The Netherlands

Received 9 March 2016 / Accepted 27 May 2016

ABSTRACT

Context. Matter flows from the central regions of quasi-stellar objects (QSOs) during their active phases are probably responsible for the properties of the super-massive black holes and those of the bulges of host galaxies. To understand how this mechanism works, we need to characterize the geometry and the physical state of the accreting matter at cosmological redshifts, when QSO activity is at its peak.
Aims. We aim to use X-ray data to probe the matter inflow at the very center of a QSO at $z = 3.62$. While complex absorption, the iron K emission line, reflection hump, and high-energy cutoff are known to be almost ubiquitous in nearby active galactic nuclei (AGN), only a few distant objects are known to exhibit some of them.
Methods. The few high-quality spectra of distant QSO were collected by adding sparse pointings of single objects obtained during X-ray monitoring campaigns. This could have introduced spurious spectral features due to source variability and/or microlensing. To avoid such problems, we decided to collect a single-epoch and high-quality X-ray spectrum of a distant AGN. We thus picked up the $z = 3.62$ QSO B1422+231, whose flux, enhanced by gravitationally lensing, is proven to be among the brightest lensed QSOs in X-rays ($F_{2-10\ \mathrm{keV}} \sim 10^{-12}$ erg s^{-1} cm^{-2}).
Results. The X-ray spectrum of B1422+231 is found to be very similar to the one of a typical nearby Seyfert galaxy. Neutral absorption is clearly detected ($N_{\mathrm{H}} \sim 5 \times 10^{21}$ cm^{-2} at the redshift of the source), while a strong absorption edge is measured at $E \sim 7.5$ keV with an optical depth of $\tau \sim 0.14$. We also find hints of the FeKα line in emission at $E \sim 6.4$ keV line ($EW \lesssim 70$ eV), and a hump is detected in the $E \sim 15-20$ keV energy band (rest frame) in excess of what is predicted by a simple absorbed power-law.
Conclusions. The spectrum can best be modeled with two rather complex models; one assumes ionized and partially covering matter along the line of sight, the other is characterized by a reflection component. We argue that reflection seems more plausible here on a statistical basis. In this scenario, the primary emission of B1422+231 is most probably dominated by the thermal Comptonization of UV seed photons in a corona with $kT \sim 40$ keV. We also detected a reflection component with relative direct-to-reflect normalization $r \sim 1$. These findings confirm that gravitational lensing is suitable for obtaining good-quality X-ray spectral information of QSOs at high-z, moreover, they support the idea that the same general picture characterizing AGN in the nearby Universe is also valid at high redshift.

Key words. galaxies: active – quasars: individual: B1422+231 – X-rays: individuals: B1422+231

1. Introduction

High-energy observations are used to study the geometry and physical condition of matter in the inner regions of active galactic nuclei (AGN) because X-rays are thought to originate from close to the central supermassive black hole (SMBH, see Antonucci 1993; Fabian 2000). In nearby Seyfert or radio galaxies, absorption that is due to cold matter along the line of sight imprints a low-energy cutoff on their X-ray spectra (Smith & Done 1996; Bassani et al. 1999; Cappi et al. 2006; Dadina 2007, 2008). In addition, most AGN observed with sufficient statistics also reveal a smoothed spectral curvature that is due to warm matter below ~4 keV (Piconcelli et al. 2005). X-ray spectra of local AGN often display emission features that are diagnostics of both the geometry of the matter infalling onto the SMBH and the emission mechanism acting to produce the high-energy emission itself (Nandra & Pounds 1994; Smith & Done 1996; Perola et al. 2002; Cappi et al. 2006; Dadina 2008; Malizia et al. 2014; Fabian et al. 2015). The most prominent of these features is the iron line at 6.4−6.9 keV. It may appear shifted in energy and skewed by relativistic effects whose strength depends on the vicinity of the line production region to the SMBH (see, Tanaka et al. 1995; Fabian et al. 2000, for a review on the topic). In addition, a hump due to the reflection of the primary emission by the matter surrounding the SMBH (Lightman & White 1988; Guilbert & Rees 1988) is usually seen at $E \sim 20-40$ keV (Perola et al. 2002; Dadina 2008). Broadband (0.1−200 keV) X-ray observations of nearby AGN also allowed us to measure

a high-energy cutoff E_C at $E \sim 70-200$ keV (Perola et al. 2002; Dadina 2008; Malizia et al. 2014; Fabian et al. 2015). This feature is expected in the so-called two-phase models for the production of the high-energy photons in radio-quiet AGN. In this scenario, optical-UV seed photons coming from the accretion disk are Comptonized into the X-ray band by the electrons forming a hot corona that sandwiches the accretion disk itself. The electrons have a thermal energy distribution, and the shape of the emerging X-ray spectrum displays a high-energy cutoff at $E_{\rm cut-off} \sim 2 \times kT_{\rm e^-}$ (Haardt & Maraschi 1993; Haardt et al. 1994; Petrucci et al. 2001).

At intermediate ($z \geq 0.1$) and high ($z \geq 1$) redshift, X-ray spectra of QSOs often display only absorption and/or the FeKα line in emission (Vignali et al. 2006), the latter being sometimes associated with Compton-thick absorbers (Vignali et al. 2010, 2014). In the framework of unified models (UM) for AGN (Antonucci 1993), at least at the zeroth order, the only differences between low- and high-z AGN should be due to cosmological evolution of the environment in which the SMBHs are embedded. Some confirmation of this picture has been effectively obtained. No strong evidence of evolution of the intrinsic X-ray properties of QSO with redshift has been observed (Vignali et al. 2005, but see Saez et al. 2008 for a suggested limited evolution of the photon index with z), while the measurement of a different evolution between absorbed and non-absorbed sources (Aird et al. 2015) seems to indicate that the circumnuclear environment may evolve with z, as expected. Similarly, the strong correlation between the X-ray photon index and the Eddington luminosity of QSOs (Lu & Yu 1999; Shemmer et al. 2006, 2008; Risaliti et al. 2009; Fanali et al. 2013; Brightman et al. 2013) has been explained in the framework of the two-phase model for the production of X-rays (Pounds et al. 1995), thus indicating that it acts both in the nearby and distant Universe. Furthermore, there have recently been claims that reflected and relativistically blurred components are also present in the X-ray spectra of some high-z ($z \geq 2$) and lensed QSO after stacking many and sparse X-ray observations of each source (Reis et al. 2014; Reynolds et al. 2014; Walton et al. 2015, but see also Chartas et al. 2007, 2016). Moreover, transient and variable absorption iron lines linked to hot and fast outflowing gas (ultra-fast outflows, aka UFO) and with quite similar characteristics were observed in the rest frame 7–10 keV spectra of both nearby Seyferts (Pounds et al. 2003; Dadina et al. 2005; Tombesi et al. 2010a,b; Gofford et al. 2013) and in an handful of bright and distant ($z \geq 1$) QSOs (Chartas et al. 2002, 2003, 2007, 2014; Lanzuisi et al. 2012; Vignali et al. 2015).

This evidence is consistent with the idea that the emission mechanism does not dramatically change over cosmic time, while some evolution with redshift may be present for the properties of the matter flows around SMBH. X-ray spectra with a high signal-to-noise ratio (S/N) are fundamental to fully characterize the environment in the central engines of AGN at high redshift and to describe how they evolve throughout cosmological time. We measure a tight correlation between the mass of the galaxies bulges and the mass of their central SMBH (Kormendy & Richstone 1995; Magorrian et al. 1998; Ferrarese & Merritt 2000; Merritt & Ferrarese 2001; Marconi et al. 2004), therefore we now know that a feedback mechanism must be at work. However, to fully understand how this works, we must constrain the physical conditions of the objects in epochs where both QSO and starburst activity were at their highest (Boyle et al. 1988; Madau et al. 1996; Brandt & Hasinger 2005, and references therein). For example, the measurement and characterization of UFOs at high-z is of crucial importance to understand when and how the feedback mechanism between the SMBH and the host galaxy bulges has set up and how it has evolved in cosmic time.

The spectroscopic X-ray studies that allowed the detection of UFO and relativistically blurred features of the most distant objects mentioned above took advantage of the fact that all the studied QSOs, except for HS 1700+6416 and PID352 (Lanzuisi et al. 2012; Vignali et al. 2015), are lensed. This means that they display magnified emission, which allows the collection of X-ray spectra of higher S/N. While waiting for the next generation of X-ray telescopes with large collecting areas such as Athena (Nandra et al. 2013), the usage of cosmic lenses may play a crucial role to extend studies at high redshift that are up to now limited to the nearby Universe. We present here the first high-quality X-ray spectrum, obtained with a single *XMM-Newton* observation of B1422+231, of a lensed and radio-loud QSO ($R_L \sim 300$, but see Sect. 3.1 for a discussion of this point) at $z = 3.62$ (Patnaik et al. 1992; Misawa et al. 2007). Its four images are all within $\sim 5''$, thus the source is point-like for *XMM-Newton*, and the magnification factor has been estimated to be between $\mu \sim 15-76$ (Kormann et al. 1994; Chiba 2002; Raychaudhury et al. 2003; Assef et al. 2011). For this work we assume a magnification factor of $\mu \sim 15-20$, which is a common range of values for the majority of the works presented above. A broad Hβ emission line has been observed in its optical spectrum, and the mass of the central SMBH has been estimated to be $\sim 5 \times 10^9$ $M_\odot$ using single-epoch CIV measurements (Greene et al. 2010); this was later confirmed using other optical lines as well (Assef et al. 2011). The X-ray spectrum of the source was previously presented in Misawa et al. (2008), who analyzed poor-quality spectra obtained with *Chandra* and *XMM-Newton*. *Chandra* was pointed at the source three times, collecting 426, 244, and 762 counts, respectively. *XMM-Newton* only observed the source for ~5 ks, and the source fell on a EPIC-pn chip gap, precluding the use the pn data. The two EPIC-MOS collected ~195 counts each (Misawa et al. 2008). In these low S/N spectra, B1422+231 displayed rather typical and almost featureless X-ray spectra with a photon index $\Gamma \sim 1.6$, with only hints of absorption ($N_{\rm H} \leq 10^{22}$ cm^{-2}) at low energies and an observed and integrated flux of $F_{2-10\ \rm keV} \sim 9 \times 10^{-13}$ erg s^{-1} cm^{-2}.

2. Data reduction and analysis

XMM-Newton pointed at B1422+231 on July 31, 2014. The data reduction was performed using the package SAS-14. The high-background periods were cleaned by excluding the first 2 ks of the pointing, so as to eliminate the first high peak of soft protons, and then we applied a filter on the count-rate (0.65 and 0.2 c/s for pn e MOS, respectively). After this filtering, we obtained a net exposure of ~65, 74.2 and 64.3 ks with pn, MOS1, and MOS2, respectively. Source counts were extracted from circular regions with radii of 30 and 40 arcsec for pn and MOS detectors, respectively, allowing us to collect 25.8, 8.2, and 7.8 k-counts with pn, MOS1, and MOS2, respectively. Background counts were extracted from source-free circular regions larger than that centered on the source but in the same chip of the source.

No variability was detected at more than 75–80% significance level, and the observed average flux is $F_{2-10\ \rm keV} \sim 10^{-12}$ erg s^{-1} cm^{-2} after the data were fit with a power law absorbed by the Galactic column density (model 1 in Table 1). This yields an observed integrated luminosity $L_{2-10\ \rm keV} \sim 6 \times 10^{46}$ erg s^{-1} (we used $H_0 = 70$ km s^{-1} Mpc^{-1}, $\Omega_{\rm M} = 0.286$ and $\Omega_\lambda = 0.714$). Errors are reported at the 90% confidence level in Table 1 and throughout the paper.

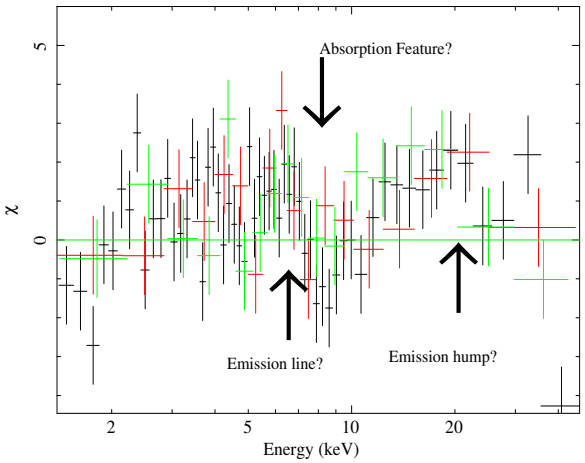

Fig. 1. Data-to-model ratio expressed in terms of standard deviations after the X-ray data were fit with a simple power-law model absorbed by the Galactic column of $N_{\rm H} = 3.2 \times 10^{20}$ cm^{-2} (Kalberla et al. 2005). Data have been rebinned so as to have 20σ significance points for clarity. EPIC-pn data points are plotted in black, MOS1 and MOS2 data points in red and green, respectively.

Table 1. Phenomenological models.

	$N_{\rm H}$	Γ	$E_{{\rm FeK}\alpha}$ ($E_{\rm edge}$)	$\sigma_{{\rm FeK}\alpha}$ ($\tau_{\rm edge}$)	$EW_{{\rm FeK}\alpha}$	χ^2/d.o.f.
	10^{21} cm^{-2}		keV (keV)	eV	eV	
1		$1.61^{+0.02}_{-0.02}$				1282/1189
2	$3.42^{+1.12}_{-1.11}$	$1.66^{+0.02}_{-0.02}$	$6.35^{+0.18}_{-0.22}$	$\leq$0.48	62^{+48}_{-34}	1256/1185
3	$2.37^{+0.10}_{-0.10}$	$1.65^{+0.02}_{-0.02}$	$6.38^{+0.13}_{-0.20}$	$\leq$0.38	$\leq$69	1228/1183
			($7.48^{+0.20}_{-0.23}$)	($0.14^{+0.04}_{-0.04}$)		

Notes. Column 1: model number; Col. 2: absorbing column in excess of the Galactic value; Col. 3: photon index; Col. 4: energy centroid of the emission Gaussian line ($E_{\rm edge}$ in the lower row of model 3); Col. 5: Line width (1σ) ($\tau_{\rm edge}$ in the lower row of model 3); Col. 6: line equivalent width; Col. 7: χ^2/degrees of freedom.

The spectral analysis of the source was performed by averaging the data over the entire good-time exposure and after grouping the data so as to have 20 counts in each spectral bin. As a sanity check, however, all the results presented below were also tested using data collected only in the first, middle, and last third of the observation, and no differences were found. This was done to detect evidence of time-dependent spectral variations, if any, which in principle might be related to either the intrinsic source variability or to the microlensing phenomenon (Paczynski 1986; Wambsganss 1990).

In Fig. 1 we show the data-to-model ratio expressed in terms of standard deviations (rest-frame energy). The data were fit using model 1 of Table 1, which consists of a simple power law absorbed (phabs model in Xspec) by Galactic column density ($N_{\rm H} = 3.2 \times 10^{20}$ cm^{-2}, Kalberla et al. 2005). The X-ray spectrum of the source clearly displays three main features: 1) a low-energy cutoff that is due to an absorption component in excess of the Galactic one; 2) a dip in counts at $E \sim 7-8$ keV plus possibly a feature in emission at $E \sim 6.5$ keV; and 3) an excess-hump at $E \sim 15-30$ keV.

To perform phenomenological tests on these features, we first added an in situ (z = 3.62) extra-column in absorption and a Gaussian line in emission (model 2 in Table 1) because they are known to be common in the X-ray spectra of AGN (Nandra & Pounds 1994; Smith & Done 1996; Vignali et al. 2006). We obtained a $\Delta\chi^2 \sim 15$ for a single parameter of interest when a cold absorber was added to model 1 of Table 1 and $\Delta\chi^2 \sim 9$ for three parameters of interest for the Gaussian line in emission. Moreover, to test the significance of the count drops at $E \sim 7.5-8$ keV, we used an absorption edge (model 3 in Table 1). Overall, we obtained that the simultaneous detection of an intrinsic absorber and of an edge is significant at more than 99%. confidence level ($\Delta\chi^2 \sim 28$ with respect to model 2 of Table 1, see also the upper panels of Fig. 2), while the strength of the detection of a Gaussian line in emission depends on the presence of the absorption edge in the underlying model: the line in emission is detected at high significance when the dip of counts at ~7.5 keV is not modeled (model 2 in Table 1), but it is detected at only ~97% confidence level when the absorption edge is modeled (see lower left panel in Fig. 2 and the parameters of model 3 in Table 1). In any case, if the width of the line is left free to vary, then we obtain that it is consistent with being narrow. The intervals of confidence reported here were calculated using the F-test, which is known to be inaccurate and, in particular, slightly optimistic (Protassov et al. 2002). Here we used the F-test probabilities as mere indications of the strength of the putative spectral features.

The parameters obtained with this simple and phenomenological modeling of the data agree well with the results previously presented by Misawa et al. (2008), who analyzed X-ray spectra with a few hundred counts. In particular, the high-energy continuum is recorded to be rather flat ($\Gamma \sim 1.6$) and absorbed by a column density of cold matter with $N_{\rm H} \sim 2.4 \times 10^{21}$ cm^{-2}. Both these values are well within the range and upper limits previously reported (Misawa et al. 2008). It is worth considering, however, that all these features are unable to account for the hump at energies higher than 10 keV (lower right panel of Fig. 2), which indicates that more complex modeling of the data is needed.

Finally, to further test the possible presence of these spectral features, we analyzed the RGS data using standard techniques. The main goal was to test the intrinsic width of the emission line. However, we obtained the poor-quality RGS spectrum (we obtained ~5000 source plus background counts, only ~20% of which originated in the source) that is plotted in Fig. 3. Using model 1 in Table 1 as underlying continuum, we thus checked that the intensity of emission line and the optical depth of the absorption edge were consistent with what has been obtained with EPIC instruments. No further constraints on the parameters of the emission line were obtained.

2.1. A complex absorbing system?

To simultaneously model the detected features, we first assumed an absorption-dominated scenario. The absorption edge measured at $E \sim 7.5$ keV might indicate that the primary emission of B1422+231 intercepts some cold or ionized matter along the line of sight that only partially covers the central engine of the source. This would introduce an underestimate of the total absorber and, thus, the appearance of the spurious edge at $E \geq 7.1$ keV in the data. To study this scenario, we used the *zxipcf* model (Reeves et al. 2008) within *Xspec*, which is able to reproduce the data well (see left panel of Fig. 4 and Table 2) after it is combined with cold absorber (see Table 2). We also used pre-compiled Xstar tables, namely mtab1e 8, 21, 22, and 25 (each obtained using an ionizing flux with power-law spectra with Γ = 2, i.e., similar to what we obtained here in the ionized absorption scenario) that have turbulence velocities from 100 to 3000 km s^{-1} and cover

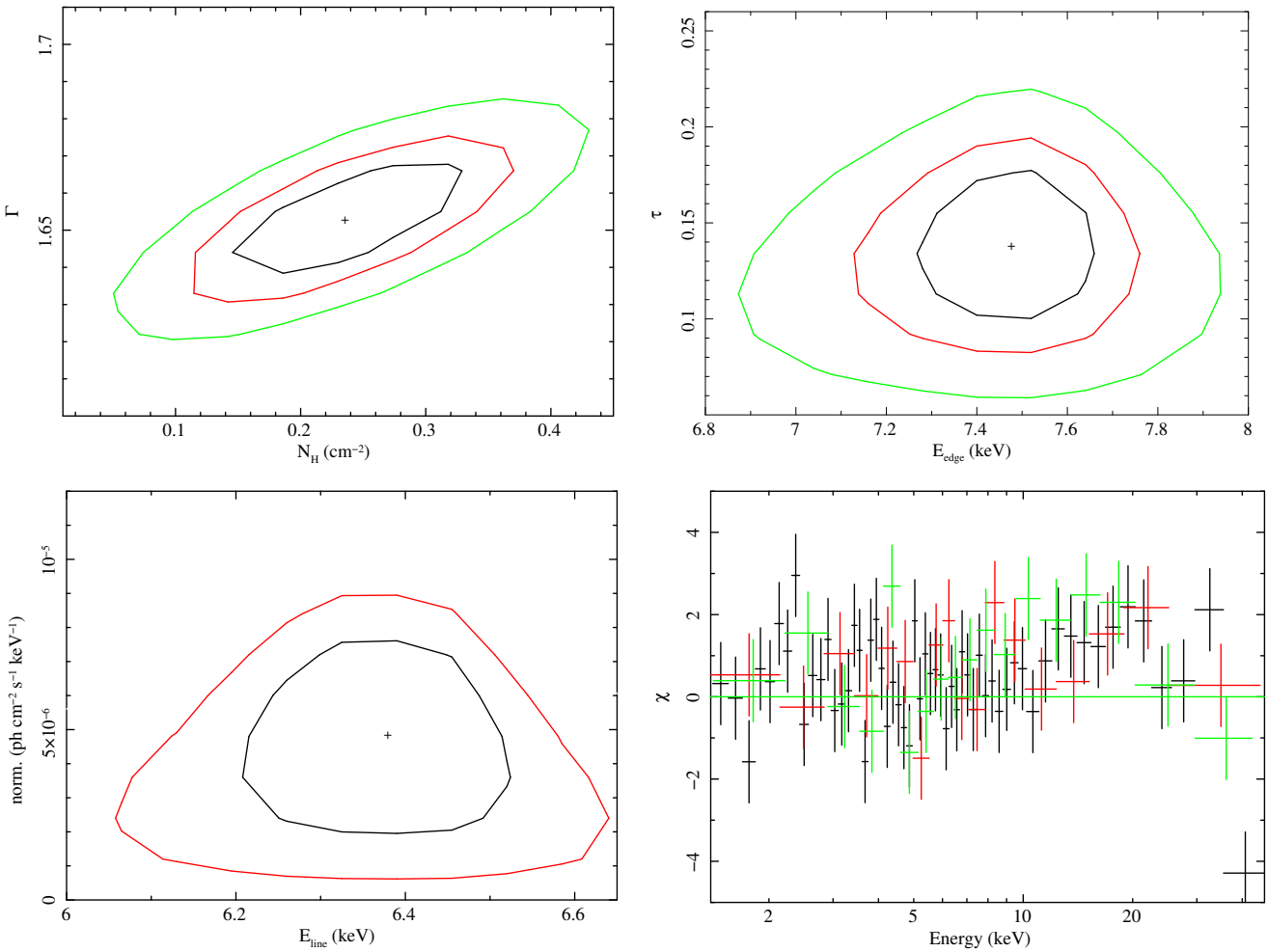

Fig. 2. Contour plots at 99, 90, and 68% confidence obtained using a model composed of a primary power-law absorbed by a cold column and by an edge at $E \sim 7.5$ keV plus a Gaussian in emission (model 3 in Table 1). *From left to right*: (*upper left panel*) photoindex Γ vs. absorbing column density ($N_{\rm H}$ in units of 10^{22}); (*upper right panel*) optical depth of the edge (τ) vs. its energy centroid; (*lower left panel*) Gaussian emission line normalization vs. its energy. In this case, only 90 and 68% confidence contours are presented since the emission Gaussian line is detected with ~97% confidence in this model and the 99% confidence contour gives only an upper limit; (*lower right panel*) data-to-model ratio expressed in terms of standard deviations. Binning and colors as in Fig. 1.

Table 2. Best-fit models: complex absorber model.

Complex absorber	$N_{\rm H,cold}$	Γ	$N_{\rm H,warm}$	C_f	Log(ξ^a)	$E_{\rm FeK\alpha}$	$\sigma_{\rm FeK\alpha}$	$EW_{\rm FeK\alpha}$	χ^2/d.o.f.
	10^{21} cm^{-2}		10^{21} cm^{-2}			keV	keV	eV	
	$8.84^{+2.16}_{-2.15}$	$1.95^{+0.09}_{-0.09}$	961^{+11}_{-12}	$0.43^{+0.08}_{-0.09}$	$2.00^{+0.21}_{-0.58}$	$6.36^{+0.36}_{-0.32}$	≤822	38^{+30}_{-30}	1207/1182

Notes. Column 1: model name; Col. 2: absorbing column in excess to the Galactic value; Col. 3: photon index; Col. 4: column density of the warm absorber; Col. 5: covering factor of the warm absorber; Col. 6: ionization parameter of the warm absorber; Col. 8: energy of the Gaussian line in emission (rest frame); Col. 8: width of the Gaussian line in emission (rest frame); Col. 9: equivalent width of the Gaussian line in emission (rest frame); and Col. 10: χ^2/degrees of freedom. $^{(a)}$ ξ expressed in erg s^{-1} cm.

wide ranges of absorbing columns ($N_{\rm H} \sim 10^{20-24}$ cm^{-2}). We tested both partial and complete absorption scenarios, but never obtained spectral fits with χ^2 values better than those obtained with *zxipcf*.

The FeKα ($E_{\rm FeK\alpha} \sim 6.4$ keV) line is only marginally detected in this case with a 90% upper limit of $EW \lesssim 70$ eV (rest frame). This value agrees well with what is expected if the line is produced in the cold absorber itself ($EW \sim 30$ eV, Makishima 1986; Leahy & Creighton 1993). It is also consistent with what is measured for the broad component of the FeKα line in nearby type I AGN ($EW \sim 75$ eV, de La Calle Pérez et al. 2010) or nearby radio-galaxies (Grandi & Palumbo 2004, 2007). Nonetheless, it is slightly lower than what is expected when a standard accretion disk in the inner core of B1422+231 is assumed ($EW \sim 100-120$ eV for type I AGN, Matt et al. 1991). The edge and hump at energies above 10 keV are here accounted for by the partially covering and warm component with high column density ($N_{\rm H} \sim 10^{24}$ cm^{-2}, Log (ξ erg s^{-1} cm) ~ 2 and $C_f \sim 0.4$). In the left panel of Fig. 4 we present the data-to-model ratio expressed in terms of standard deviation as a function of rest-frame energy. Some features may still be present at $E \sim 15$ keV (rest frame). It is worth noting, however, that this

Table 3. Best-fit models: reflection model.

Reflection dominated	N_H	Γ	$E_{cut-off}$	r	θ	χ^2/d.o.f.
	10^{21} cm^{-2}		keV		degrees	
	$4.57^{+1.79}_{-1.73}$	$1.81^{+0.08}_{-0.07}$	80^{+34}_{-19}	$1.10^{+0.31}_{-0.31}$	45^{fixed}	1207/1186

Notes. Column 1: model name; Col. 2: absorbing column in excess to the Galactic value; Col. 3: photon index; Col. 4: high-energy cutoff (rest frame); Col. 5: relative reflected-to-direct emission normalization; Col. 6: inclination angle; and Col. 7: χ^2/degrees of freedom.

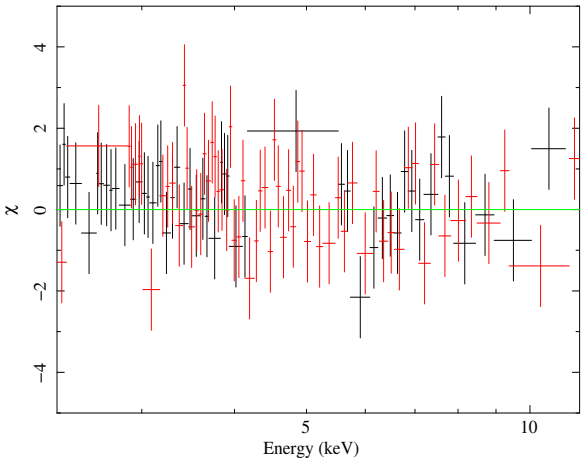

Fig. 3. Rest-frame data-to-model ratio expressed in terms of standard deviations after the RGS data are fit with model 1 of Table 1. Data have been rebinned so as to have 20 source plus counts per energy bin. RGS1 and RGS2 data points are plotted in black and red, respectively.

corresponds to $E \sim 2-3$ keV in the observed frame, that is, to an energy band where instrumental absorption edges might well be important[1] (but see the end of Sect. 2.2 for a more detailed discussion of this topic).

2.2. Is there a reflection component?

Both the ~7.5 keV edge and the ~15−20 keV hump might be due to a reflection component in the X-ray spectrum of B1422+231. To test this, we used the *Pexmon* model in *Xspec* (Nandra et al. 2007), which consistently models the continuum hump at energies above 10 keV and the associated emission lines (but see also Murphy & Yaqoob 2009 for a discussion of the possible underestimation of the reflection component when slab geometries are assumed for the reflector, as done in *pexmon*). Given the limited statistics available, we fixed some of the variables of the model: the inclination angle of the reflecting system with respect to the line of sight was fixed to $\Theta = 45°$ and the abundance of all elements were set equal to solar (when it was left free to vary, the inclination angle was statistically unconstrained, while the abundance was found to be larger than ~0.3 solar at 90% confidence level with a $\Delta\chi^2 \sim 0.5$ for one more parameter of interest and for a best value Abund ~ 0.95 solar). As reported in Table 3, this model provides an excellent fit of the data (see also right panel of Fig. 4). As often observed in nearby Seyfert galaxies and radio galaxies, the slope of the primary power-law steepens when the reflection component is added and reaches values ($\Gamma \sim 1.8$) that are commonly observed in the nearby Universe (Dadina 2008; Cappi et al. 2006) and are perfectly consistent with predictions in the two-phase scenario (Haardt et al. 1997). Moreover, taking advantage of the high redshift of B1422-231, we were able to measure a high-energy cutoff ($E_c \sim 80$ keV, see Table 3 and the left panel of Fig. 5). The reflection component is measured at a good significance level (right panel of Fig. 5), and the relative intensity of the reflected component with respect to the direct continuum is $r \sim 1$, which is consistent with a 2π coverage of the reflector. We also tested the hypothesis of relativistically blurred reflection by smearing the *Pexmon* component with a relativistic kernel (namely kdblur in Xspec), but the data did not statistically require the addition of such an effect.

As for the complex absorber, some residuals remain at ~15 keV even in the reflection scenario (see right panel of Fig. 4). We first tried to test its statistical importance. Since the residuals in the reflection scenario seem more peaked than for the complex absorption, we first added a broad Gaussian in emission and found that the fit improved by only very little ($\Delta\chi^2 \sim 4$ for three more parameters of interest). This indicates that the addition of such feature is not required by the data, statistically speaking. The energy of the line, moreover, is found to be $E \sim 2.7$ keV (observed frame), and this suggests that at least part of the residuals may be due to calibration problems around the AU M edge as a result of the mirror coating ($E \sim 2.5$ keV). On a more reliable physical basis, we also tested adding another reflection component that is due, for example, to the contribution of the putative torus and/or accretion disk, without finding any significant improvement in the fit. When we checked for the ionization state of the reflector using the XILLVER model in Xspec (García et al. 2014), we found that the ionization parameter is consistent with zero and lower than Log (ξ erg s^{-1} cm) ≤ 2.2. We finally stress here that some sort of spectral noise may be also introduced by the fact that we are observing a quadruply lensed object. This means that the light paths of the four images may be different, and for this reason, each of the four images may show slightly different X-ray spectra.

2.3. Searching for hints of outflowing matter

We also tested for possible outflowing matter both in the absorption and reflection scenarios that could be responsible for blueshifted absorption at energies close to that of the absorption edge. Following Tombesi et al. (2010a,b) and Chartas et al. (2003), we first modeled this component with a simple Gaussian in absorption. The method consists of performing blind searches over the entire X-ray spectra of a narrow absorption Gaussian line and then checking the statistical strength of the found feature by performing Monte Carlo simulations. The simulations always found that the significance of the absorption lines was slightly lower than that calculated with the F-test (Tombesi et al. 2010a,b). Here we adopted a simplified version of this procedure, without Monte Carlo simulations, because we found that the feature is not required by the data (see Fig. 6), statistically speaking. We had a similar result when we adopted a P-Cygni profile to simultaneously model the emission line and

[1] See *XMM-Newton* Users' Handbook at http://xmm.esac.esa.int

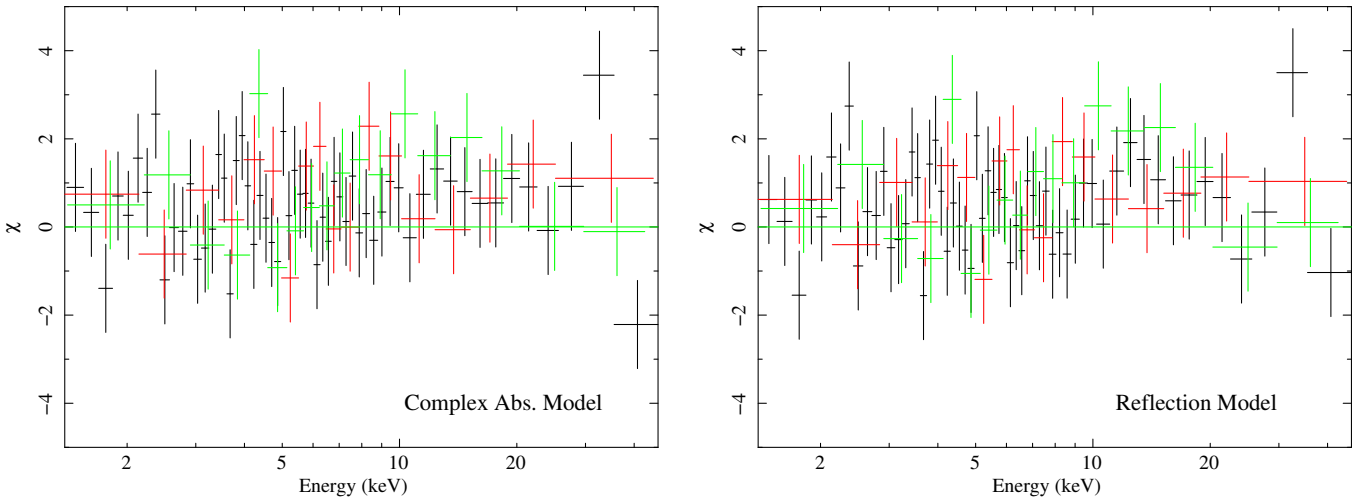

Fig. 4. Data-to-model ratios in terms of standard deviations when the data are fit by a complex absorption and reflection (*left panel*) and a reflection model (*right panel*). Binning and colors as in Fig. 1.

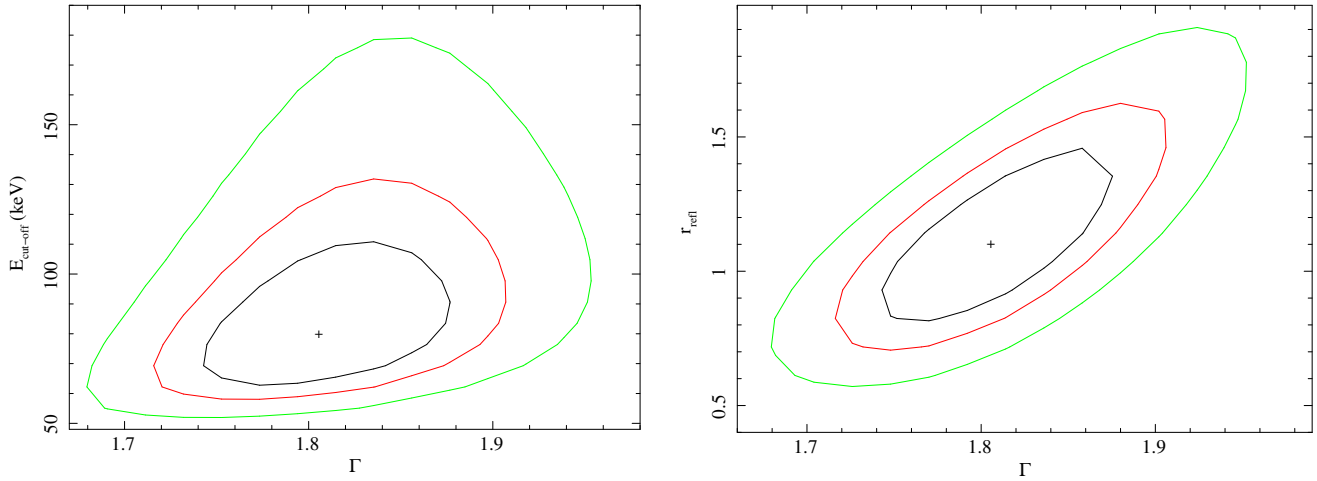

Fig. 5. Confidence contours of the high-energy cutoff vs. photon index (*left panel*) and relative normalization of the reflected component vs. photon index (*right panel*) as measured when the X-ray data of B1422+231 are modeled using *Pexmon* (Nandra et al. 2007).

the absorption edge as has recently been observed in PDS 456 (Nardini et al. 2015). In this case, we used the model by Done et al. (2007). This component, when added to the absorbed power-law, is not able to model all the spectral complexity observed between 6−8 keV (rest frame), while when it is added to the complex absorption and reflection scenario, it does not allow to significantly improve the modeling of the data ($\Delta\chi^2 \lesssim 2.5$ for three more parameters of interest when the P-Cygni profile model is added to the complex absorber scenario).

3. Discussion

We presented the complex X-ray spectrum of the distant (z = 3.62) and lensed QSO B1422+231. The magnification factor $\mu \sim 15-20$ (Kormann et al. 1994; Assef et al. 2011) and the long *XMM-Newton* pointing allowed us to obtain an X-ray spectrum with very high quality considering the distance of the target ($D_{\rm L}$ = 32.2 Gpc). The *XMM-Newton* pointing allowed us to collect ∼40 kcounts in a single observation (considering the three EPIC instruments onboard *XMM-Newton*) in the 0.3−10 keV energy range (observer frame). This is one of the best single-epoch X-ray spectrum of high-z QSO ever obtained. To our knowledge, the only observations of high-redshift QSOs of comparable quality are those obtained with *XMM-Newton* for the lensed QSO APM 08279+5255 (z = 3.92, see Saez & Chartas 2011, for a list of X-ray observations of the source) with ∼16.5 kcounts for their deepest *XMM-Newton* observation.

The integrated X-ray flux recorded during the *XMM-Newton* pointing presented here is $F_{2-10\ \rm keV} \sim 10^{-12}$ erg s^{-1} cm^{-2}, which corresponds to an unobscured luminosity of $L_{2-10\ \rm keV} \sim 7.3 \times 10^{46}$ erg/s. The source, however, is known to be magnified by a factor $\mu \sim 15-20$ (Kormann et al. 1994; Assef et al. 2011). We can thus estimate the intrinsic luminosity to be $L_{2-10\ \rm keV} \sim 5 \times 10^{45}$ erg s^{-1}, which translates into $L_{\rm bol} \sim 4.5-9.4 \times 10^{46}$ erg s^{-1} after the bolometric correction is also taken into account ($k_{\rm bol}$ ranges between ∼9−15 depending on the spectral index, which is here found to range between $\Gamma \sim 1.65-1.95$ depending on the modeling of the data, Marchese et al. 2012). This implies that the source apparently emits at ∼7−15% of its Eddington luminosity ($L_{\rm Edd} \sim 6.5 \times 10^{47}$ erg s^{-1}). The measured 2−10 keV luminosity is very typical of what is measured for lensed objects (Misawa et al. 2008) and is also comparable to what is measured for a sample of radio-quiet QSOs observed with *XMM-Newton* ($L_{2-10\ \rm keV} \sim 0.4-7 \times 10^{46}$ erg s^{-1}, Page et al. 2005) at a redshift of between $z \sim 2-4$. It is at the lowest end of the luminosity ranges measured for radio-loud objects ($L_{2-10\ \rm keV} \sim 0.5-70 \times 10^{46}$ erg s^{-1}, Page et al. 2005), suggesting that the

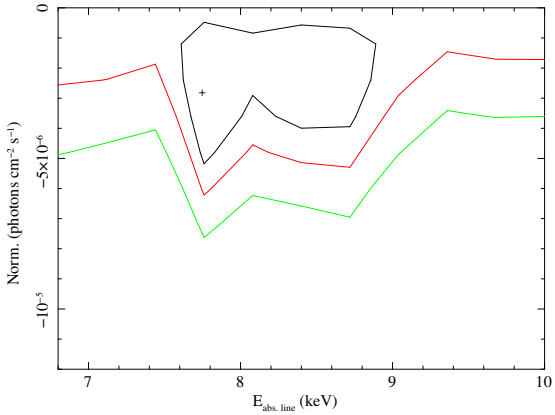

Fig. 6. Confidence contours of the normalization of a Gaussian line in absorption vs. its energy centroid. The baseline model is here the reflection dominated one presented in Table 3. The inclusion of the absorption line yields to $\Delta\chi^2 \sim 2.5$ for two more parameters of interest. The line width has been fixed to $\sigma = 10$ eV.

source brightness does not experience extreme boosting effects in X-rays.

The spectral analysis of the X-ray data clearly demonstrates that the spectrum of B1422+231 is complex and shows some highly significant features such as a low-energy cutoff that is due to absorption, a deep dim of counts at $E \sim 7$−7.5 keV (rest frame), and a hump at $E \sim 20$−30 keV plus a low-energy cutoff. We also have indications of an iron emission line at $E \sim 6.4$ keV. All this evidence indicates the possible presence of a partial coverer (complex absorption scenario) and/or a reflection component (reflection scenario), that is, toward the possibility that we might be observing a Seyfert-like X-ray spectrum. This scenario is also suggested by the detection of absorption in X-rays that is due to intervening matter, as is observed in nearby Seyferts. This component is apparently at odds with predictions by the unified models of AGN (Antonucci 1993) when considering broad emission lines in the optical spectrum of B1422+231, and thus its type I nature is taken into account. It is worth considering, however, that it is common in the local Universe as well to observe type I Seyferts that are absorbed in X-rays (see, for example, NGC 4151 and of NGC 4051, Warwick et al. 1993; and Ponti et al. 2006, respectively). In recent years, moreover, long-term monitoring of sources that have been displaying characteristics of type I objects from optical-UV to X-rays for decades showed that these sources may suddenly change their X-ray properties to those typical of type II objects and maintain them for years (see, for example, H0557-385 and NGC 5548, Coffey et al. 2014; Kaastra et al. 2014).

The complex X-ray spectrum of B1422+231, moreover, seems to be in contrast with the definition of the source as radio-loud (Misawa et al. 2008) and, thus, a strong or even dominant jet component producing an almost featureless spectrum may also be expected in X-rays. We therefore investigated the radio-loudness of B1422+231 using the parameter defined by Kellermann et al. (1989), $R = f_{5\ \mathrm{GHz}}/f_{4400\ \text{Å}}$, where the optical wavelength and the radio frequency are in the source rest frame. Typical radio-loudness values are >100 for radio-loud QSOs and <10 for radio-quiet QSOs. The rest-frame 5 GHz flux density was computed from the 1.4 GHz flux density value of 352 mJy reported by Tinti et al. (2005), extrapolated to a 5 GHz rest frame assuming a radio power-law slope of $\alpha = 0.9$ as reported in Orienti et al. (2007), where $S_\nu \propto \nu^{-\alpha}$. The rest frame 4400 Å flux density was computed by adopting the composite QSO spectrum presented in Vanden Berk et al. (2001) to convert the broadband Sloan Digital Sky Survey (SDSS) *ugriz* measurements into the flux density at the rest wavelength of 4400 Å (see Vignali et al. 2003 for further details). We obtain $R \approx 90$, which indicates that B1422+231 is only moderately radio loud.

On the other hand, the very steep radio continuum measured by Orienti et al. (2007) with the VLA ($\alpha \sim 0.9$) might indicate that the source is highly inclined in the plane of the sky. In this case, the radio emission should be dominated by the lobes and not by the jet, which does not point toward us, thus reconciling the radio- and X-ray properties of the target. Nonetheless, VLBI imaging of B1422+231 does not allow detecting any extended structures at more than ∼1−2 milliarcsec (Dallacasa, priv. comm.). This means that the physical dimensions of the radio source are smaller than ∼10−20 kpc at the redshift of the source. We cannot probe to scales small enough to show that B1422+231 has intrinsic small radio-emitting regions such as those found in CoreG or FR0 sources (Baldi et al. 2015) since the angular resolution of the VLBI is at the limit of the typical dimension of such sources. CoreG radio-emitting regions have typical dimensions ≲10−20 kpc, and we would need to be able to probe even smaller angular scales to exclude extended emission on the scales of ∼1−3 kpc that are typical of FR0 (Baldi et al. 2015). Overall, the radio properties of B1422+231 prevent us from firmly assessing the nature of the source. While the polarization in the radio-band and the radio flux variability, even if very weak, may suggest a blazar nature of the source, the steady radio spectral shape and the low polarization at low frequencies indicate that B1422+231 may be a genuinely young radio source (Orienti et al. 2007; Orienti & Dallacasa 2008). To this evidence, we add that, as most probably occurs in the optical, the X-ray band is also dominated by the emission from a disk component, which implies that the jet does not dominate at all frequencies. We finally note that 4C74.26, the closest powerful radio-loud QSO, also displays a Seyfert-like X-ray spectrum (Grandi et al. 2006; Fukazawa et al. 2011).

3.1. Two best-fit scenarios

As mentioned above, the X-ray spectrum of B1422+231 is strongly characterized by features similar to those commonly observed in nearby Seyfert galaxies, which might indicate that the primary emission is affected by complex absorption and/or reflection.

In the complex-absorption scenario, we obtain that the primary engine is absorbed by a cold absorber with a column density of $N_\mathrm{H} \sim 10^{22}$ cm^{-2} that completely covers the region in which the X-ray photons originate plus an ionized ($\xi \sim 100$ erg s^{-1} cm and $N_\mathrm{H} \sim 10^{24}$ cm^{-2}) partial coverer that hides only ∼40% of this region ($C_f \sim 0.4$). When we adopt this model, we obtain that the putative FeKα line is not detected at a 99% confidence level ($EW \lesssim 70$ eV at 90% confidence), but its strength is still consistent with expectations for the observed absorbing column (Makishima 1986; Leahy & Creighton 1993; Matt et al. 1991). The partial covering of the central engine suggests that the core of B1422+231 hosts intervening clouds that are able to partially block the line of sight. This is similar to observations in nearby AGNs. In some Seyfert galaxies, clouds, probably the same as are forming the broad line regions, have been observed to cross the line of sight and produce eclipses (Risaliti et al. 2007). Similarly, in other objects, the changes in absorbing column have been associated with outflowing clouds (Coffey et al. 2014; Kaastra et al. 2014; Arav et al. 2015). The

changes in the absorption properties are thought to be responsible for at least part of the well-known AGN variability seen in X-rays (see, for example, NGC 1365, Risaliti et al. 2005, 2009; see also Miller et al. 2008, 2010; Markowitz et al. 2014). In this scenario, assuming that the density of these clouds is typical of the broad line regions BLR ($n \sim 10^9$ cm^{-3}) and taking the luminosity of the source obtained above ($\sim 5 \times 10^{46}$ erg s^{-1}), they are at $d \sim 7 \times 10^{17}$ cm, which corresponds to $\sim 5000 r_g$ or ~ 0.1 pc from the source of X-ray photons. This is at a distance of only about half of the expected average distance of the BLR for a QSO of the given $L_{\rm bol}$ (in accordance to what has been found for the eclipsing cloud in NGC 1365 $d \sim 100 r_g$, Risaliti et al. 2007). An even looser limit is obtained following Tarter et al. (1969). Under the assumption that $d_{\rm max} \lesssim L_{\rm ion}/\xi N_{\rm H}$. If $L_{\rm ion} = L_{2-10\ \rm keV}$, we obtain the $d_{\rm max} \sim 4 \times 10^{18}$ cm, which is one order of magnitude larger than what was obtained before. In both cases, the values obtained agree well with results obtained by Tombesi et al. (2012), who constrained the production region of UFOs detected in nearby AGN, and by Markowitz et al. (2014), who constrained the distance of the clouds forming the torus. It is worth considering, however, that in this picture eclipsing episodes are responsible for the different observed X-ray flux states at which the sources are detected and that these episodes are generally related to cold clouds (Risaliti et al. 2007; Markowitz 2014; Coffey et al. 2014; Kaastra et al. 2014). Based on archival data, we are unable to detect any variations of the absorbing column density. Moreover, the X-ray flux of B1422+231 observed during the 2014 observation is not significantly different from previously measurements, that is to say, no long-term variability has been detected. We also failed to detect significant short-term variability, and no dominating flux dip is measured, which means that we have no indications of eclipsing episodes. It is worth considering, however, that the detection of strong variability, especially on short timescales, is here disfavored by both the source redshift and by the SMBH mass ($M_{\rm SMBH} \sim 5 \times 10^9\ M_\odot$, Greene et al. 2010).

Under the reflection scenario we obtained a value of χ^2 almost identical to the one obtained with the complex absorption model, but with fewer free parameters (see Table 2). After the spectral complexities were taken into account with *Pexmon*, the spectral index was found to be steep ($\Gamma \sim 1.8$) and in agreement with average measurements in the AGN in the nearby Universe (Perola et al. 2002; Cappi et al. 2006; Dadina 2008). This value is well within the range of the photon index predicted for Seyfert galaxies (Haardt et al. 1994) and observed in QSO at intermediate and high redshift for objects with an Eddington luminosity similar to that of B1422+231 (Brigthman et al. 2013). Most interestingly, the adoption of the *Pexmon* model (Nandra et al. 2007) allowed us to consistently fit the hump that is due to the reflection of the primary continuum onto the matter surrounding the central engine and the associated emission lines. In this framework, taking advantage of the source redshift and of the *XMM-Newton* sensitivity, we were able to measure both the high-energy cutoff ($E_{\rm c} \sim 80$ keV) and the normalization between the primary emission and the reflected component ($r \sim 1$) that indicates that the reflecting matter covers $\sim$50% of the sky as seen by the source of X-ray photons. These values are well within the range measured in nearby Seyferts (Perola et al. 2002; Dadina 2008). To our knowledge, this is the first AGN for which we are able to perform such measurements at $z \geq 3$ (but see Lanzuisi et al. 2016, for the possible detection of such features in the X-ray spectrum of a $z \sim 2$ QSO). This allowed us to probe the geometry of the accreting matter around an SMBH at ages when the QSOs activity was at its peak, thus possibly opening new opportunities for testing the SMBH-galaxy feedback and formation models (King & Pounds 2015, and references therein). The detection of the high-energy cutoff, moreover, allowed us to infer the temperature of the putative Comptonizing corona ($kT \sim \frac{E_{\rm cut-off}}{2}$) and its optical depth, which, following Eq. (1) in Petrucci et al. (2001), is $\tau \sim 0.3$ for B1422+231. It is worth noting, however, that the kT values derived from *Pexmon*, that is, derived from *Pexrav* (Magdziarz & Zdziarski 1995), must be considered to be, in general, underestimated, while τ is overestimated. The reason is the spherical and isotropic geometry assumed in this model. A more realistic slab and anisotropic geometry of a Comptonization model is expected to provide different values of $E_{\rm c}$ and τ, and the value presented above must be taken with cautions.

4. Summary and conclusions

We summarize our findings as follows: the coupling of the magnification factor that is due to gravitational lensing and the sensitivity of *XMM-Newton* allowed us to obtain a very high-quality X-ray spectrum of a QSO at $z = 3.62$. This technique thus proved to be useful to directly probe the physical properties of the matter surrounding the SMBH at high redshift, that is, at the peak of both QSO and starburst activities. The source X-ray spectrum is certainly complex, displaying strong and highly significant signatures of both emission and absorption components. The spectrum is equally well fit by either a complex absorption model or a reflection model.

Even though we have no firm indication of which of the two best-fit models proposed here is correct, we favor the reflection-dominated interpretation because we did not detect any hint of variability on either short or long timescales so that passing and partially absorbing clouds seem to be disfavored, and because the reflection model is better on a pure statistical basis, allowing us to obtain a good modeling of the data with fewer parameters. In this scenario, we stress that we have been able to measure the strength of the reflection component ($r \sim 1$) and the temperature of the Comptonizing corona by inferring that the geometry and the physical state of the matter around the SMBH hosted in the $z = 3.62$ B1422+231 QSO are similar to what has been measured in nearby Seyfert galaxies.

Acknowledgements. We thank the anonymous referee for the helpful comments that helped us to improve the manuscript. This work is based on observations obtained with *XMM-Newton*, an ESA science mission with instruments and contributions directly funded by ESA Member States and the USA (NASA). M.D. thanks Paola Grandi, Daniele Dallacasa for useful discussions. M.D. and M.C. aknowledge financial support from the Italian Space Agency under grant ASI-INAF I/037/12/0 and extended PRIN INAF 2012. GL acknowledges financial support from the CIG grant "eEASY" No. 321913, from ASI-INAF 2014-045-R.0 and ASI/INAF I/037/12/0–011/13 grants. G.P. thanks the DLR: the Bundesministerium für Wirtschaft und Technologie/Deutsche Zentrum für Luft-und Raumfahrt (BMWI/DLR, FKZ 50 OR 1408).

References

Aird, J., Coil, A. L., Georgakakis, A., et al. 2015, MNRAS, 451, 1892
Antonucci, R. 1993, ARA&A, 31, 473
Arav, N., Chamberlain, C., Kriss, G. A., et al. 2015, A&A, 577, A37
Assef, R. J., Denney, K. D., Kochanek, C. S., et al. 2011, ApJ, 742, 93
Baldi, R. D., Capetti, A., & Giovannini, G. 2015, A&A, 576, A38
Bassani, L., Dadina, M., Maiolino, R., et al. 1999, ApJS, 121, 473
Boyle, B. J., Shanks, T., & Peterson, B. A. 1988, MNRAS, 235, 935
Brandt, W. N., & Hasinger, G. 2005, ARA&A, 43, 827
Brightman, M., Silverman, J. D., Mainieri, V., et al. 2013, MNRAS, 433, 2485
Cappi, M., Panessa, F., Bassani, L., et al. 2006, A&A, 446, 459
Chartas, G., Brandt, W. N., Gallagher, S. C., & Garmire, G. P. 2002, ApJ, 579, 169

Chartas, G., Brandt, W. N., & Gallagher, S. C. 2003, ApJ, 595, 85
Chartas, G., Eracleous, M., Dai, X., Agol, E., & Gallagher, S. 2007, ApJ, 661, 678
Chartas, G., Hamann, F., Eracleous, M., et al. 2014, ApJ, 783, 57
Chartas, G., Rhea, C., Kochanek, C., et al. 2016, Astron. Nachr., 337, 356
Chiba, M. 2002, ApJ, 565, 17
Coffey, D., Longinotti, A. L., Rodríguez-Ardila, A., et al. 2014, MNRAS, 443, 1788
Dadina, M. 2007, A&A, 461, 1209
Dadina, M. 2008, A&A, 485, 417
Dadina, M., Cappi, M., Malaguti, G., Ponti, G., & de Rosa, A. 2005, A&A, 442, 461
de La Calle Pérez, I., Longinotti, A. L., Guainazzi, M., et al. 2010, A&A, 524, A50
Done, C., Sobolewska, M. A., Gierliński, M., & Schurch, N. J. 2007, MNRAS, 374, L15
Fabian, A. C., Iwasawa, K., Reynolds, C. S., & Young, A. J. 2000, PASP, 112, 1145
Fabian, A. C., Lohfink, A., Kara, E., et al. 2015, MNRAS, 451, 4375
Fanali, R., Caccianiga, A., Severgnini, P., et al. 2013, MNRAS, 433, 648
Ferrarese, L., & Merritt, D. 2000, ApJ, 539, L9
Fukazawa, Y., Hiragi, K., Mizuno, M., et al. 2011, ApJ, 727, 19
García, J., Dauser, T., Lohfink, A., et al. 2014, ApJ, 782, 76
Gofford, J., Reeves, J. N., Tombesi, F., et al. 2013, MNRAS, 430, 60
Grandi, P., & Palumbo, G. G. C. 2004, Science, 306, 998
Grandi, P., & Palumbo, G. G. C. 2007, ApJ, 659, 235
Grandi, P., Malaguti, G., & Fiocchi, M. 2006, ApJ, 642, 113
Greene, J. E., Peng, C. Y., & Ludwig, R. R. 2010, ApJ, 709, 937
Guilbert, P. W., & Rees, M. J. 1988, MNRAS, 233, 475
Haardt, F., & Maraschi, L. 1993, ApJ, 413, 507
Haardt, F., Maraschi, L., & Ghisellini, G. 1994, ApJ, 432, L95
Haardt, F., Maraschi, L., & Ghisellini, G. 1997, ApJ, 476, 620
Kaastra, J. S., Kriss, G. A., Cappi, M., et al. 2014, Science, 345, 64
Kalberla, P. M. W., Burton, W. B., Hartmann, D., et al. 2005, A&A, 440, 775
Kellermann, K. I., Sramek, R., Schmidt, M., Shaffer, D. B., & Green, R. 1989, AJ, 98, 1195
King, A., & Pounds, K. 2015, ARA&A, 53, 115
Kormann, R., Schneider, P., & Bartelmann, M. 1994, A&A, 286, 357
Kormendy, J., & Richstone, D. 1995, ARA&A, 33, 581
Lanzuisi, G., Giustini, M., Cappi, M., et al. 2012, A&A, 544, A2
Lanzuisi, G., Perna, M., Comastri, A., et al. 2016, A&A, 590, A77
Leahy, D. A., & Creighton, J. 1993, MNRAS, 263, 314
Lightman, A. P., & White, T. R. 1988, ApJ, 335, 57
Lu, Y., & Yu, Q. 1999, ApJ, 526, L5
Madau, P., Ferguson, H. C., Dickinson, M. E., et al. 1996, MNRAS, 283, 1388
Magdziarz, P., & Zdziarski, A. A. 1995, MNRAS, 273, 837
Magorrian, J., Tremaine, S., Richstone, D., et al. 1998, AJ, 115, 2285
Makishima, K. 1986, The Physics of Accretion onto Compact Objects, 266, 249
Malizia, A., Molina, M., Bassani, L., et al. 2014, ApJ, 782, L25
Marchese, E., Della Ceca, R., Caccianiga, A., et al. 2012, A&A, 539, A48
Marconi, A., Risaliti, G., Gilli, R., et al. 2004, MNRAS, 351, 169
Markowitz, A. G., Krumpe, M., & Nikutta, R. 2014, MNRAS, 439, 1403
Matt, G., Perola, G. C., & Piro, L. 1991, A&A, 247, 25
Merritt, D., & Ferrarese, L. 2001, MNRAS, 320, L30
Miller, L., Turner, T. J., & Reeves, J. N. 2008, A&A, 483, 437
Miller, L., Turner, T. J., Reeves, J. N., & Braito, V. 2010, MNRAS, 408, 1928
Misawa, T., Charlton, J. C., Eracleous, M., et al. 2007, ApJS, 171, 1
Misawa, T., Eracleous, M., Chartas, G., & Charlton, J. C. 2008, ApJ, 677, 863
Murphy, K. D., & Yaqoob, T. 2009, MNRAS, 397, 1549
Nandra, K., & Pounds, K. A. 1994, MNRAS, 268, 405
Nandra, K., O'Neill, P. M., George, I. M., & Reeves, J. N. 2007, MNRAS, 382, 194
Nandra, K., Barret, D., Barcons, X., et al. 2013, ArXiv e-prints [arXiv:1306.2307]
Nardini, E., Reeves, J. N., Gofford, J., et al. 2015, Science, 347, 860
Orienti, M., & Dallacasa, D. 2008, A&A, 479, 409
Orienti, M., Dallacasa, D., & Stanghellini, C. 2007, A&A, 475, 813
Paczynski, B. 1986, ApJ, 301, 503
Page, K. L., Reeves, J. N., O'Brien, P. T., & Turner, M. J. L. 2005, MNRAS, 364, 195
Patnaik, A. R., Browne, I. W. A., Walsh, D., Chaffee, F. H., & Foltz, C. B. 1992, MNRAS, 259, 1
Perola, G. C., Matt, G., Cappi, M., et al. 2002, A&A, 389, 802
Petrucci, P. O., Haardt, F., Maraschi, L., et al. 2001, ApJ, 556, 716
Piconcelli, E., Jimenez-Bailón, E., Guainazzi, M., et al. 2005, A&A, 432, 15
Protassov, R., van Dyk, D. A., Connors, A., Kashyap, V. L., & Siemiginowska, A. 2002, ApJ, 571, 545
Ponti, G., Miniutti, G., Fabian, A. C., Cappi, M., & Palumbo, G. G. C. 2006, Astron. Nachr., 327, 1055
Pounds, K. A., Done, C., & Osborne, J. P. 1995, MNRAS, 277, L5
Pounds, K. A., Reeves, J. N., King, A. R., et al. 2003, MNRAS, 345, 705
Raychaudhury, S., Saha, P., & Williams, L. L. R. 2003, AJ, 126, 29
Reeves, J., Done, C., Pounds, K., et al. 2008, MNRAS, 385, L108
Reis, R. C., Reynolds, M. T., Miller, J. M., & Walton, D. J. 2014, Nature, 507, 207
Reynolds, M. T., Walton, D. J., Miller, J. M., & Reis, R. C. 2014, ApJ, 792, L19
Risaliti, G., Elvis, M., Fabbiano, G., Baldi, A., & Zezas, A. 2005, ApJ, 623, L93
Risaliti, G., Elvis, M., Fabbiano, G., et al. 2007, ApJ, 659, L111
Risaliti, G., Young, M., & Elvis, M. 2009, ApJ, 700, L6
Saez, C., & Chartas, G. 2011, ApJ, 737, 91
Saez, C., Chartas, G., Brandt, W. N., et al. 2008, AJ, 135, 1505
Shemmer, O., Brandt, W. N., Netzer, H., Maiolino, R., & Kaspi, S. 2006, ApJ, 646, L29
Shemmer, O., Brandt, W. N., Netzer, H., Maiolino, R., & Kaspi, S. 2008, ApJ, 682, 81
Smith, D. A., & Done, C. 1996, MNRAS, 280, 355
Tanaka, Y., Nandra, K., Fabian, A. C., et al. 1995, Nature, 375, 659
Tarter, C. B., & Salpeter, E. E. 1969, ApJ, 156, 953
Tinti, S., Dallacasa, D., de Zotti, G., Celotti, A., & Stanghellini, C. 2005, A&A, 432, 31
Tombesi, F., Cappi, M., Reeves, J. N., et al. 2010a, A&A, 521, A57
Tombesi, F., Sambruna, R. M., Reeves, J. N., et al. 2010b, ApJ, 719, 700
Tombesi, F., Cappi, M., Reeves, J.N., & Braito, V. 2012, MNRAS, 422, L1
Vanden Berk, D. E., Richards, G. T., Bauer, A., et al. 2001, AJ, 122, 549
Vignali, C., Brandt, W. N., & Schneider, D. P. 2003, AJ, 125, 433
Vignali, C., Brandt, W. N., Schneider, D. P., & Kaspi, S. 2005, AJ, 129, 2519
Vignali, C., Alexander, D. M., & Comastri, A. 2006, MNRAS, 373, 321
Vignali, C., Alexander, D. M., Gilli, R., & Pozzi, F. 2010, MNRAS, 404, 48
Vignali, C., Mignoli, M., Gilli, R., et al. 2014, A&A, 571, A34
Vignali, C., Iwasawa, K., Comastri, A., et al. 2015, A&A, 583, A141
Walton, D. J., Reynolds, M. T., Miller, J. M., et al. 2015, ApJ, 805, 161
Wambsganss, J. 1990, Ph.D. Thesis, Münich
Warwick, R. S., Sembay, S., Yaqoob, T., et al. 1993, MNRAS, 265, 412